Valence States in $CeVO_4$ and $Ce_{0.5}Bi_{0.5}VO_4$ Probed by Density Functional Theory Calculations and X-ray Photoemission Spectroscopy

J. P. Allen, N. M. Galea and G. W. Watson*
School of Chemistry & CRANN, Trinity College Dublin, Dublin 2, Ireland

R.G. Palgrave

Department of Chemistry, University College London, Christopher Ingold Building, 20 Gordon Street, London WC1H 0AJ, UK

J.M. Kahk and D.J. Payne

Department of Materials, Imperial College London, Exhibition Road, London SW7 2AZ, UK

M.D.M. Robinson, G. Field, A. Regoutz and R.G.Egdell

University of Oxford, Department of Chemistry, Inorganic Chemistry Laboratory, South Parks Road, Oxford, OX1 3QR, UK

Abstract

Ce is one of the few lanthanide elements to exhibit well-defined (III) and (IV) oxidation states in solid state environments and there is therefore ambiguity as to whether $CeVO_4$ should be formulated as $Ce(III)V(V)O_4$ or $Ce(IV)V(IV)O_4$. To address this question $CeVO_4$ and $Ce_{0.5}Bi_{0.5}VO_4$ have been studied by density functional theory calculations and X-ray photoemission spectroscopy. A peak above the main O 2*p* valence band in photoemission is attributed to localised Ce 4*f* states, in agreement with the calculations which show occupation of Ce 4*f* states. The Ce 3*d* core level spectrum is diagnostic of Ce(III) with no sign of a peak associated with $4f^0$ final states that are characteristic of Ce(IV) compounds. The experimental and theoretical results thus confirm that both compounds contain Ce(III) and V(V), rather than Ce(IV) and V(IV). In agreement with experiment, the calculations also show that the tetragonal zircon phase adopted by $CeVO_4$ is more stable for $Ce_{0.5}Bi_{0.5}VO_4$ than the monoclinic clinobisvanite phase adopted by $BiVO_4$, so that formation of the stereochemically active Bi(III) lone pairs is suppressed by Ce doping.

Keywords.

Electronic structure; vanadates; X-ray photoelectron spectroscopy; lone pairs.

1. Introduction

$CeVO_4$ has aroused widespread interest in recent years by virtue of its application as an oxidation catalyst[1-2], photocatalyst[3-4], gas sensor material[5] and pigment[6]. The formation (or not) of the $CeVO_4$ phase also impinges on the operation of V_2O_5 catalysts supported on CeO_2. In addition quaternary vanadate phases involving the doping of $BiVO_4$ with rare earths including Ce have attracted attention in their own right as potential photocatalytic materials[4] with a performance superior to that of $BiVO_4$ itself.

$BiVO_4$ has three different polymorphs: orthorhombic pucherite,[7] tetragonal dreyerite,[8] and monoclinic clinobisvanite.[8] The monoclinic phase is most stable thermodynamically at room temperature and also displays the most promising photocatalytic activity.[6, 8-10] This phase belongs to space group *I*2/*b* and also contains BiO_8 dodecahedra and VO_4 tetrahedra, as shown in figure 1(a). $CeVO_4$ has two different polymorphs: a tetragonal zircon-type phase and a monoclinic huttonite-type phase, the latter being metastable at room temperature.[11] Zircon-type $CeVO_4$ (space group $I4_1/amd$) is composed of CeO_8 dodecahedra and VO_4 tetrahedra, as shown in figure 1(b). The dodecahedra of the $BiVO_4$ and $CeVO_4$ structures are quite different. In contrast to $CeVO_4$, the dodecahedra around the Bi atoms are observed to be significantly distorted with four different bond lengths: 2×2.346 Å , 2×2.375 Å, 2×2.528 Å and 2×2.605 Å bonds.[12] This creates a weakly layered structure stacked in the *c* direction with the bonds shorter than 2.4 Å on one side of the Bi ions and the bonds longer than 2.5 Å on the other. This coordination geometry is suggestive of stereochemically active Bi(III) lone pairs and leads to ferroelectric behavior.[8] However the formation of the directional lone pairs requires hybridisation of Bi 6*s* states with O 2*p* states at the top of the valence band.[13] Since the 6*s* of Bi states lie almost 10 eV below the top of the valence band[14-16], the hybridisation is relatively weak

and the driving force for structural distortion is quite small. As will emerge below, $Ce_{1-x}Bi_xVO_4$ solid solutions with $x \leq 0.5$ are most stable in the tetragonal zircon phase with almost regular coordination around the Bi ions.

The solid state chemistry of lanthanide compounds is usually dominated by the trivalent (III) oxidation state. However cerium forms a wide range of Ce(IV) compounds and both CeO_2 and Ce_2O_3 are well characterised. Given that vanadium forms oxides in both the pentavalent (V) and tetravalent (IV) oxidation states there is therefore an ambiguity as to whether $CeVO_4$ should be formulated as Ce(III)V(V)O_4 or Ce(IV)V(IV)O_4. On the basis of density functional theory (DFT) calculations using a range of functionals at different levels of sophistication, Sauer and co-workers[17] concluded that $CeVO_4$ is a $4f^1$ Ce(III) compound, although the energy difference between Ce(III)V(V)O_4 and Ce(IV)V(IV)O_4 was found to be very small and dependent on the on-site Coulomb parameter for Ce introduced into functionals involving a "+*U*" term. However, inclusion of a "+*U*" for Ce but not for V must invariably favor localisation of excess charge on Ce rather than V. Moreover, the assignment of valence states is a matter that ideally should be explored by both theory and experiment. Against this background we have initiated a study of rare earth vanadates and $BiVO_4$ doped with rare earth ions using core and valence X-ray photoemission spectroscopy as an experimental probes of electronic structure and report here results for $CeVO_4$ and $Ce_{0.5}Bi_{0.5}VO_4$. These are compared with similar results for $BiVO_4$. The spectroscopic data are compared with DFT calculations involving the generalised gradient approximation (GGA) with the addition of an onsite *U* electron repulsion parameter for *both* V and Ce, so as not to tip the balance in favour of localisation on Ce. Comparison of the placement of the Ce 4 *f* levels relative to the valence band edge in the calculations with experimental data provides a critical test of the appropriateness or otherwise of the "+*U*" value selected for Ce.

2. Experimental

$Ce_{0.5}Bi_{0.5}VO_4$, $CeVO_4$ and $BiVO_4$ were prepared by ceramic solid synthesis. CeO_2 (Sigma-Aldrich 99.99%), Bi_2O_3 (Sigma-Aldrich 99.999%) and V_2O_5 (Sigma-Aldrich 99.99%) were ground in an agate mortar and pestle in appropriate stoichiometric quantities, pelletized between 13 mm diameter tungsten carbide dies under a 5 ton loading for 5 minutes and then fired at 600 °C for 16 hours. The products were reground and refired at 900 °C for an additional 16 hours. X-ray diffraction patterns confirmed a phase-pure monoclinic solid had been prepared in the case of $BiVO_4$, whereas both $Ce_{0.5}Bi_{0.5}VO_4$ and $CeVO_4$ adopted the tetragonal zircon structure. Lattice parameters derived from the powder patterns for $CeVO_4$ and $Ce_{0.5}Bi_{0.5}VO_4$ are given in table 1. The values for $CeVO_4$ are in good agreement with those reported previously.[18] $CeVO_4$ and $Ce_{0.5}Bi_{0.5}VO_4$ were further characterised by measurement of the magnetic susceptibilities over a temperature range between of 5 K to 300 K in a Quantum Design MPMS XL magnetometer. The susceptibility χ_m was fitted to an expression of the sort:

$$\frac{1}{\chi_m} = \frac{T - \theta}{C}$$

Where θ is the Weiss constant and C is the Curie constant, which determines the effective magnetic susceptibility μ_{eff}. The plots of inverse susceptibility against temperature were linear down to about 150 K for $CeVO_4$ and to 100 K for $Ce_{0.5}Bi_{0.5}VO_4$, below which temperatures non-linearities associated with crystal field splitting of the Ce 4*f* levels were observed.[19] The Weiss constants were negative (table 1), indicative of incipient antiferromagnetic interactions, with a more negative value for the parent compound $CeVO_4$. This difference would be anticipated since the magnetic centres are more dilute in $Ce_{0.5}Bi_{0.5}VO_4$. The effective magnetic moment of 2.89 μ_B found for $CeVO_4$ was larger than the published value of 2.64 μ_B[19] but this can be attributed to the fact that our regression was restricted to a narrower temperature range than in reference 19 in

order to ensure better linearity. The effective magnetic moments are much bigger than would be expected for a V^{4+} $3d^1$ system and but are quite close to the value predicted for the $^2F_{5/2}$ ground state of Ce^{3+}.

The majority of the X-ray photoemission spectra were measured in a Scienta ESCA 300 spectrometer housed in Daresbury Laboratory UK. This incorporates a rotating anode Al Kα (hν = 1486.6 eV) X-ray source, a 7 crystal X-ray monochromator and a 300mm mean radius spherical sector electron energy analyser with parallel electron detection using channel plates, a scintillation screen and a camera. The X-ray source was run with 200 mA emission current and 14 kV anode bias, whilst the analyser operated at 150 eV pass energy. Gaussian convolution of the analyser resolution with a linewidth of 260 meV for the X-ray source gives an effective instrument resolution of 400 meV. Binding energies are referenced to the Fermi energy of a silver sample regularly used to calibrate the spectrometer. Further spectra were measured in a Thermo Scientific K-Alpha spectrometer located at University College London, UK. This spectrometer also uses an Al Kα source but with a lower power input of 72 W. The X-rays are microfocused at source to give a spot size on the sample of 400 microns. The monochromator is comprised of a single toroidal quartz crystal set in a Rowland circle with radius 250 mm. The analyser is a double focusing 180 degree hemisphere with mean radius 125 mm and was run in constant analyser energy (CAE) mode with the pass energy set to 50 eV, giving an overall instrument resolution of about 0.5 eV . The detector is a 128 channel position sensitive detector.

3. Computational

All calculations within this study were performed using the periodic density functional theory (DFT) code VASP[20-21], which employs a plane-wave basis set to describe the valence electronic states. The Perdew-Burke-Ernzerhof (PBE)[22] gradient-corrected functional was used to treat the

exchange and correlation. Interactions between the cores (Bi:[Xe], Ce: [Xe], V:[Ar] and O:[He]) and the valence electrons were described using the projector-augmented wave [23] (PAW) method, with the Bi 5d state included in the valence shell. To counteract the problems associated with the DFT self-interaction error (SIE)[24], which can artificially delocalise *d*- and *f*-electrons, a GGA+*U* methodology is employed.[25] This approach effectively adds a penalty to delocalisation, correcting for on-site Coulombic interactions, and has been demonstrated to give improved descriptions of the atomic and electronic structures for a large range of systems.[26-35] In this study, *U* values of 4.5 and 4.0 eV are applied to the Ce 4*f* and V 3*d* states, respectively. A value of 4.5 eV has been widely used for modelling Ce ions, showing good agreement to experimental data for $CeVO_4$, Ce_2O_3 and CeO_2 systems.[17, 36-37] A *U* of 4.0 eV has been shown to provide good atomic and electronic structure data for V_2O_5.[26] To the best of our knowledge, this represents the first study to model $CeVO_4$ with *U* terms for both Ce and V. The inclusion of a *U* term for V is important because in V_2O_5 itself excess electrons introduced by oxygen vacancies or Li doping remain itinerant at the GGA level of theory and only become localised (as is found experimentally) when a *U* term is added for V.

Structural optimisation of both the pure and the mixed vanadate systems were performed at a series of volumes in order to calculate the equilibrium lattice parameters. In each case, the atomic positions, lattice vectors and cell angles were allowed to relax, while the total volume was held constant. The resulting energy-volume curves were fitted to the Murnaghan [38] equation of state to obtain the equilibrium bulk cell volume. This approach avoids the isotropic problems of Pulay stress and changes in basis set which can accompany volume changes in plane wave calculations. [39] Convergence with respect to the plane-wave energy cut-off and *k*-point sampling were checked, with a cut-off of 500 eV and a Monkhorst-Pack 6 × 6 × 6 mesh found to be

sufficient for all systems. Structural optimizations were deemed to be converged when the forces on each ion were less than 0.001 eV $Å^{-1}$. All calculations were spin polarized to ensure the correct magnetic ground state was found.

When comparing the computational results with experimental photoemission data it is necessary to account for the effects of instrumental and phonon broadening. Gaussian convolution was applied to the calculated densities of states using a profile with a full width at half maximum (FWHM) of 0.8 eV. For states in the lower part of the valence band the contribution of lifetime broadening also becomes significant. This can be accounted for by additional convolution with a Lorentzian lineshape, whose FWHM scales with the square of the binding energy; in this case the best agreement was obtained when FWHM = 0.008 E^2 where E is expressed in electronvolts. The justification for the E^2 dependence of the inverse lifetime of the final state of the photoemission process arises as follows: whilst the Einstein coefficient for spontaneous emission scales as E^3, this is offset by a decrease in the matrix elements connecting the states at the Fermi level and the hole state with increasing binding energy. Whilst exact E^2 scaling is only obtained in the case of Fermi liquid theory, as an approximation it seems to work well even in non-metallic systems. [40-43]

4. Results and discussion

4.1 Computational results for pure materials

The calculated structural parameters for the pure orthovanadates are given in Table 2. For $BiVO_4$, the calculated cell parameters show some deviations from experimental values[12] ranging between -0.10% and +1.84%. Although a slightly expanded cell often emerges using a GGA+*U* methodology, the differences in this case appear to reflect specific problems with treatment of

the BiO_8 dodecahedra. In the experimental structure the bond lengths range between 2.346 Å and 2.605 Å. In the calculations the dodecahedra, do not show this level of distortion, with minimum and maximum bond lengths of 2.447 Å and 2.511 Å respectively. Earlier calculations using GGA methodologies have also failed to reproduce the full extent of structural distortion.[16, 44]

The calculated cell parameters for $CeVO_4$ are also seen to show differences from the experimental values. However, the deviations are less pronounced than for $BiVO_4$, with the vectors and bond lengths differing from experiment[18] by between 0.79% and 1.87%. As will be seen below, $CeVO_4$ contains Ce(III) ions and the unpaired 4*f* electrons give rise to different possible magnetic structures. All possible ferromagnetic (FM) and antiferromagnetic (AFM) configurations within the unit cell were modelled to ensure that the magnetic ground state was found. Although the AFM structure shown in figure 2 was found to have the lowest absolute energy and was therefore used to determine ground state properties, it is only 0.5 meV more stable than a FM configuration and both magnetic solutions have similar structural and electronic properties. This indicates that the material should remain paramagnetic down to very low temperature, consistent with magnetic susceptibility data.[11] As noted in the experimental section the negative Weiss constant found for this material is indicative of antiferromagnetic interactions,[45] although there is no transition into a magnetically ordered state down to 5K.

The calculated total electronic density of states (EDOS) and partial (ion and *l*-quantum number decomposed) electronic density of states (PEDOS) for the two materials are shown in figure 3. For $BiVO_4$ (figure 3(a)), the top of the valence band is seen to be dominated by O 2*p* character. The main contribution from the Bi 6*s* states is observed approximately 9.2 eV below the valence band maximum (VBM), with a small amount of in-phase mixing with O 2*p* states. The Bi 6*s* states are also seen to contribute to the VBM to give an O 2*p* – Bi 6*s* antibonding state.

Further mixing with Bi 6*p* states to give a well-defined directional lone pair as found in compounds such as tetragonal PbO and SnO is however very muted, as would be expected from the lack of pronounced asymmetry in the calculated Bi-O bond lengths.[13] The situation is in fact reminiscent of cubic PbS[46] and SnTe,[47] as well as the hypothetical rock salt-structured PbO[48-49] where stereochemically active lone pairs do not develop. Two peaks are observed for the V 3*d* states, centred at -4.7 and -3.1 eV, both of which show mixing with O 2*p* states. The peak at -4.7 eV also shows mixing with the Bi 5*p* states. The bottom of the conduction band is composed primarily of empty Bi 5*p*, V 3*d* and O 2*p* states. The composition of the PEDOS is consistent with previous computational[16] and experimental results.[50] From the EDOS, the band gap is estimated to be ~2.4eV, which is slightly larger than in a previous computational study and close to experimental values (2.4-2.5 eV). [9, 51-52]

The EDOS for $CeVO_4$, figure 3(b), shows similarities to that of $BiVO_4$ in that the valence band is dominated by O 2*p* states. The V 3*d* states are again seen to mix with the O 2*p* states at the bottom of the O 2*p* band but there is very little mixing between empty Ce 5*d* states and O 2*p* states. Moreover, the O 2*p* band does not extend up to the VBM as in the Bi-analogue. This is due to a new band derived from the Ce 4*f* states which makes up the VBM. The occupation of Ce 4*f* states immediately suggests that $CeVO_4$ should be formulated as $Ce(III)V(V)O_4$, in agreement with earlier work.[17] The top of the occupied O 2*p* band is separated from the bottom of the Ce 4*f* band by 1.1eV. The bottom of the conduction band is composed primarily of empty V 3*d* and O 2*p* states. From the EDOS, the band gap is estimated to be ~2.0 eV, which compares well to the experimental value of 1.8 eV. [6] There is almost no mixing between Ce 4*f* states and O 2*p* states so that the former remain atomic-like.

4.2 Computational results for solid solutions

Following simulation of the pure bulk structures, solid solutions were considered. This involved replacing half the Bi ions in monoclinic $BiVO_4$ with Ce or half the Ce ions in tetragonal $CeVO_4$ with Bi, giving two structural forms for the solid solution $Ce_{0.5}Bi_{0.5}VO_4$. All configurations of cation substitution within the unit cell were explored, with the minimum energy structures for the two forms shown in figure 4. As can be seen, the structural motifs for the pure equivalents shown in figure 1 are retained in the two structures with no dramatic rearrangements or relaxations. Different magnetic structures were again trialled for the two $Ce_{0.5}Bi_{0.5}VO_4$ structures. For the monoclinic structure, the lowest in energy was found to be a FM configuration, as shown in figure 3(a), although it was only marginally more stable than an AFM arrangement. For the tetragonal structure, an AFM solution was the most stable, as shown in figure 3(b). This is again consistent with the negative Weiss constant found by analysis of magnetic data. The energies of the FM monoclinic and the AFM tetragonal $Ce_{0.5}Bi_{0.5}VO_4$ systems per MVO_4 unit were found to be -43.28 eV and -43.44 eV respectively, which indicates that the solid solution is more stable in the zircon-type AFM $CeVO_4$ structure. This is in agreement with earlier experiments where $Ce_{1-x}Bi_xVO_4$ solid solutions with $x \leq 0.5$ were found to crystallise in the zircon structure.[6] Preference for the tetragonal zircon structure in $Ce_{0.5}Bi_{0.5}VO_4$ is further confirmed in the present experiments, which also reveal that AFM interactions are dominant, albeit with a negative Weiss constant numerically smaller than that of $CeVO_4$. As with the parent compound there is no transition to a magnetically ordered state above 5 K.

The structural parameters of the energy minimised unit cells are given in table 3. The introduction of Ce into monoclinic $BiVO_4$ produces a small *increase* in the cell volume within the monoclinic phase, whereas introduction of Bi into the tetragonal phase leads to small

decrease in cell volume. These changes are not consistent with ionic radii of 1.17 Å and 1.14 Å for 8-coordinate Bi(III) and Ce(III) appearing in the much-cited tabulation due to Shannon.[53] However two considerations lead to the conclusion that Ce(III) has a bigger effective ionic radius than Bi(III), at least in these materials. Firstly the volume per formula unit from both theory and experiment is bigger for tetragonal $CeVO_4$ than monoclinic $BiVO_4$ and the average M(III)-O bond length in $CeVO_4$ (2.4838 Å) is slightly bigger than in $BiVO_4$ (2.4635 Å) – see table 1. Second the experimental and computational cell parameters for tetragonal $Ce_{0.5}Bi_{0.5}VO_4$ found in the present work are slightly *smaller* than those found for the parent compound $CeVO_4$ – see tables 1,2 and 3. In fact the computational and experimental results are in agreement showing an experimental decrease in cell volume of −1.50% on doping Bi(III) into $CeVO_4$ compared to a decrease of −2.02% predicted in the calculations.

The calculated EDOS and PEDOS for the two solid solution structures are given in figure 6. The electronic structure is seen to be broadly similar for the two polymorphs, apart from the differing spin polarisations resulting from the magnetic structures. Furthermore, they are also very similar to those seen for the parent materials and can be viewed as being a combination of those of $BiVO_4$ and $CeVO_4$. To compare the EDOS to the pure materials, we can consider two energy separations: that between the occupied O 2*p* valence band and the Ce 4*f* band; and the optical gap of the material, between the occupied Ce 4*f* peak and the bottom of the conduction band. For monoclinic $Ce_{0.5}Bi_{0.5}VO_4$ these energies are 0.7 eV and 2.0 eV, respectively, whereas for tetragonal $Ce_{0.5}Bi_{0.5}VO_4$ they are found to be 1.2 eV and 1.9 eV, respectively.

For $BiVO_4$ this means that the addition of Ce causes an overall increase in the gap between the occupied Bi 6*s* - O 2*p* states at the top of the valence band and the bottom of the conduction band by 0.3 eV, but a reduction in the fundamental band gap by 0.4 eV due to the

additional Ce 4*f* states. For $CeVO_4$, the addition of Bi is seen to cause a small reduction of around ~0.1eV in the separation between the Ce 4*f* states and the conduction band states. Experimentally the bandgap of tetragonal $Bi_{0.5}Ce_{0.5}VO_4$ is found to be 1.5 eV, whereas the gap of $CeVO_4$ is 1.8 eV.[6] Thus the reduction in bandgap found in the calculations is confirmed by experiment, at least qualitatively.

4.3 Valence and core photoemission

Valence band X-ray photoemission spectra of $BiVO_4$, $Ce_{0.5}Bi_{0.5}VO_4$ and $CeVO_4$ are shown in the bottom panels of figure 7. The spectra are in each case dominated by the main O 2*p* valence band, which peaks at around 6 eV binding energy. For $BiVO_4$ and $Ce_{0.5}Bi_{0.5}VO_4$ an additional feature associated with the states of dominant Bi 6*s* atomic character is found below the bottom of the valence band, maximising at about 12 eV binding energy. As expected this peak is two times stronger for $BiVO_4$ than for $Ce_{0.5}Bi_{0.5}VO_4$. For both $Ce_{0.5}Bi_{0.5}VO_4$ and $CeVO_4$ a further sharp peak is found above the top of the main valence band. This corresponds to the Ce 4*f* states and is stronger for $CeVO_4$ than $Ce_{0.5}Bi_{0.5}VO_4$. The main O 2*p* valence band of $BiVO_4$ shows distinctive shoulders to both low and high binding energies. These are less apparent in spectra of $Ce_{0.5}Bi_{0.5}VO_4$ and $CeVO_4$ and it is also notable that the O 2*p* valence band becomes progressively narrower as Bi is replaced with Ce.

The changes observed experimentally are reproduced by the calculations, as seen by comparison between the experimental data and the calculated electronic densities of states also shown in figure 7. In particular the main valence band becomes narrower as Bi is replaced with Ce. This appears to reflect the fact that valence orbitals of Ce (Ce 4*f* and Ce 5*d*) hybridise much less strongly with O 2*p* states than the Bi 5*p* states, which make a pronounced contribution to the

main O 2*p* valence band. The calculations also generate states of dominant Ce 4*f* and Bi 6*s* character above and below the main O 2*p* valence band. However the absolute intensity of the Ce 4*f* structure and to a lesser extent the Bi 6*s* states does not match that found experimentally. This can be attributed to the fact that the one electron cross sections for ionisation of Bi 6*s* and Ce 4*f* states are calculated to be respectively 1100 Barns and 650 Barns as compared to a calculated one electron cross section of only 60 Barns for O 2*p* states.[54] Weighting the partial densities of states with one electron cross section appears to overcompensate this discrepancy as evident from figure 7, where the Ce 4*f* structure is obviously much too strong compared to the O 2*p* states. Similar problems have been found in comparing cross section weighted partial densities of states with experimental Al Kα XPS data in a number of other oxide systems including PbO_2,[55-57] In_2O_3[58] and CdO.[59] A possible explanation recently put forward to explain the disagreement for CdO[59] recognises that when an ionisation cross section is low it is intrinsically susceptible to "intensity borrowing" mediated by a breakdown of the independent electron approximation. Specifically it was suggested that the very low O 2*p* cross section at X-ray photon energies is enhanced by interchannel coupling (a many body effect arising from electron correlation and involving configuration interaction in the final i.e. continuum state of the photoionization process) with the much stronger O 2*s* or O 1*s* ionizations. Drube *et al.*[60] have recently shown that interchannel coupling of this sort may be significant well above threshold but will eventually decline at very high photon energy. In support of this idea we note that the agreement between theory and experiment does significantly improve with increasing photon energy in the hard XPS regime (hν>3 keV) for CdO.

Ce 3*d* core XPS spectra for $Ce_{0.5}Bi_{0.5}VO_4$ and $CeVO_4$ are shown in figure 8, along with data for a reference sample of CeO_2. For the two vanadates the Ce $3d_{5/2}$ and $3d_{3/2}$ peaks are each

split into a doublet, giving spectra which are much simpler in appearance than that found for CeO_2. The complex spectral profile for Ce(IV)O_2 has been discussed in detail many times before, [61-66] but in outline the spectrum reflects both pronounced O 2*p* – Ce 4*f* covalent mixing in the initial state and final state screening involving charge transfer from an occupied O 2*p* state into a 4*f* state upon creation of a Ce 3*d* core hole. The spectra may then be simulated using cluster models with three distinct final state 4*f* configurations, namely $4f^0$, $4f^1$ and $4f^2$. Corresponding spectra of Ce(III) compounds are much simpler because there is no covalent mixing in the initial state which in cluster calculations is dominated by a single $4f^1$ configuration. The two peak structure of the $3d_{5/2}$ and $3d_{3/2}$ core lines then arises from the possibility of final state screening to give a $4f^2$ configuration. The spectra of $Ce_{0.5}Bi_{0.5}VO_4$ and $CeVO_4$ showed no indication of peaks associated with a $4f^0$ final state. Thus the Ce 3*d* spectra are $Ce_{0.5}Bi_{0.5}VO_4$ and $CeVO_4$ are diagnostic of Ce(III) with no evidence for the coexistence of the Ce(IV) state.

Similarly the V 2*p* spectra for $BiVO_4$, $Ce_{0.5}Bi_{0.5}VO_4$ and $CeVO_4$ show in figure 9 suggest that there is no change in the vanadium valence state when Bi is replaced with Ce: the V $2p_{3/2}$ remains relatively sharp and symmetric with no significant change in core binding energy. Thus we must conclude that V retains its maximal oxidation state throughout the series. In summary then core XPS provides unambiguous evidence that $Ce_{0.5}Bi_{0.5}VO_4$ and $CeVO_4$ are Ce(III) + V(V) compounds with no hint of V(IV) and Ce(IV).

5. Conclusions.

The combined theoretical and experimental study of $Ce_{0.5}Bi_{0.5}VO_4$ and $CeVO_4$ confirms that both these compounds contain Ce(III) and V(V). This result is consistent with the established standard

reduction potentials for V(V) and Ce(IV) in aqueous solution which are respectively +1.44 V and +1.00 V i.e. Ce(IV) will oxidise V(IV) to V(V). Moreover incorporation of Ce into $BiVO_4$ to give $Ce_{0.5}Bi_{0.5}VO_4$ is sufficient to suppress the structural distortion associated with stereochemically active lone pairs in the former material. A surprising result to emerge from both theory and experiment is that Ce(III) has a bigger effective ionic radius than Bi(III) in these materials, a result at variance with the standard tabulations due to Shannon[53], although the results are consistent with the earlier tabulation of ionic radii due to Shannon and Prewitt[67] which gives 8-coordinate Bi(III) an ionic radius of 1.11 Å that is smaller than the value of 1.14 Å for 8-coordinate Ce(III).

Acknowledgements

This theoretical work (J.P.A, N.M.G and G.W.W) has emanated from research conducted with the financial support of Science Foundation Ireland (SFI) under Grant Number 06/IN.1/I92 and 12/IA/1414. Calculations were performed on the Lonsdale and Crusher supercomputers as maintained by Trinity Centre for High Performance Computing, and the Stokes supercomputer maintained by the Irish Center for High-End Computing. R.G.P. acknowledges EPSRC grant EP/K014099/1. D.J.P. acknowledges support from the Royal Society (UF100105). J.M.K. acknowledges support from the EPSRC for a Doctoral Prize Studentship. D.J.P. and R.G.P. acknowledge the support of the Materials Design Network.

References.

1. Luo, F.; Jia, C. J.; Liu, R.; Sun, L. D.; Yan, C. H., Nanorods-Assembled $CeVO_4$ Hollow Spheres as Active Catalyst for Oxidative Dehydrogenation of Propane. *Materials Research Bulletin* **2013,** *48* 1122-1127.

2. Martinez-Huerta, M. V.; Deo, G.; Fierro, J. L. G.; Banares, M. A., Operando Raman-Gc Study on the Structure-Activity Relationships in V^{5+}/CeO_2 Catalyst for Ethane Oxidative Dehydrogenation: The Formation of $CeVO_4$. *J Phys. Chem. C* **2008,** *112* 11441-11447.

3. Bellakki, M. B.; Baidya, T.; Shivakumara, C.; Vasanthacharya, N. Y.; Hegde, M. S.; Madras, G., Synthesis, Characterization, Redox and Photocatalytic Properties of $Ce_{1-x}Pd_xVO_4$ ($0 \leq x \leq 0.1$). *Applied Catalysis B-Environmental* **2008,** *84* 474-481.

4. Xu, H.; Wu, C. D.; Li, H. M.; Chu, J. Y.; Sun, G. S.; Xu, Y. G.; Yan, Y. S., Synthesis, Characterization and Photocatalytic Activities of Rare Earth-Loaded $BiVO_4$ Catalysts. *Appl. Surf. Sci.* **2009,** *256* 597-602.

5. Chen, L. M., Hydrothermal Synthesis and Ethanol Sensing Properties of $CeVO_4$ and $CeVO_4$-CeO_2 Powders. *Materials Letters* **2006,** *60* 1859-1862.

6. Dolgos, M. R.; Paraskos, A. M.; Stoltzfus, M. W.; Yarnell, S. C.; Woodward, P. M., The Electronic Structures of Vanadate Salts: Cation Substitution as a Tool for Band Gap Manipulation. *J. Solid State Chem.* **2009,** *182* 1964-1971.

7. Qurashi, M. M.; Barnes, W. H., The Structure of Pucherite, $BiVO_4$. *American Mineralogist* **1953,** *38* 489-500.

8. Sleight, A. W.; Chen, H.-Y.; Ferretti, A., Crystal Growth and Structure of $BiVO_4$. *Materials Research Bulletin* **1979,** *14* 1571-1581.

9. Sayama, K.; Nomura, A.; Arai, T.; Sugita, T.; Abe, R.; Yanagida, M.; Oi, T.; Iwasaki, Y.; Abe, Y.; Sugihara, H., Photochemical Decomposition of Water into H_2 and O_2 on Porous $BiVO_4$ Thin-Film Electrodes under Visible Light and Significant Effect on Agion Treatment. *J. Phys. Chem. B* **2006,** *110* 11352-11360.

10. Tokunaga, S.; Kato, H.; Kudo, A., Selective Preparation of Monoclinic and Tetragonal $BiVO_4$ with Scheelite Structure and Their Photocatalytic Properties. *Chem. Mater.* **2001,** *13* 4624-4628.

11. Yoshimura, M.; Sata, T., A New Monoclinic Phase of Cerium Orthovanadate ($CeVO_4$). *Bull. Chem. Soc. Jpn.* **1969,** *42* 3195-3198

12. Liu, J.-C.; Chen, J.-P.; Li, D.-Y., Crystal Structure and Optical Observations of $BiVO_4$. *Acta Physica Sinica* **1983,** *32* 1053-1060.

13. Walsh, A.; Payne, D. J.; Egdell, R. G.; Watson, G. W., Stereochemistry of Post-Transition Metal Oxides: Revision of the Classical Lone Pair Model. *Chem. Soc. Rev.* **2011,** *40* 4455-4463.

14. Walsh, A.; Watson, G. W.; Payne, D. J.; Edgell, R. G.; Guo, J. H.; Glans, P. A.; Learmonth, T.; Smith, K. E., Electronic Structure of the Alpha and Delta Phases of Bi_2O_3: A Combined *Ab Initio* and X-Ray Spectroscopy Study. *Phys. Rev. B* **2006,** *73* 235104.

15. Payne, D. J.; Egdell, R. G.; Walsh, A.; Watson, G. W.; Guo, J.; Glans, P. A.; Learmonth, T.; Smith, K. E., Electronic Origins of Structural Distortions in Post-Transition Metal Oxides: Experimental and Theoretical Evidence for a Revision of the Lone Pair Model. *Phys. Rev. Lett.* **2006,** *96* 157403.

16. Walsh, A.; Yan, Y.; Huda, M. N.; Al-Jassim, M. M.; Wei, S. H., Band Edge Electronic Structure of $BiVO_4$: Elucidating the Role of the Bi 5s and V 3d Orbitals. *Chem. Mat.* **2009,** *21* 547-551.

17. Da Silva, J. L. F.; Ganduglia-Pirovano, M. V.; Sauer, J., Formation of the Cerium Orthovanadate $CeVO_4$: DFT+U Study. *Phys. Rev. B* **2007,** *76* 125117.

18. Chakoumakos, B. C.; Abraham, M. M.; Boatner, L. A., Crystal Structure Refinements of Zircon-Type MVO_4 (*M* = Sc, Y, Ce, Pr, Nd, Tb, Ho, Er, Tm, Yb, Lu). *J. Solid State Chem.* **1994,** *109* 197-202.

19. Guo, M. D.; Aldred, A. T.; Chan, S. K., Magnetic-Susceptibility and Crystal-Field Effects of Rare-Earth Ortho-Vanadate Compounds. *J. Phys. Chem. Solids* **1987,** *48* 229-235.

20. Kresse, G.; Furthmüller, J., Efficiency of *Ab Initio* Total Energy Calculations for Metals and Semiconductors Using a Plane-Wave Basis Set. *Comput. Mater. Sci.* **1996,** *6* 15-50.

21. Kresse, G.; Hafner, J., Ab-Initio Molecular-Dynamics Simulation of the Liquid-Metal Amorphous-Semiconductor Transition in Germanium. *Phys. Rev. B* **1994,** *49* 14251-14269.

22. Perdew, J. P.; Burke, K.; Ernzerhof, M., Generalized Gradient Approximation Made Simple. *Phys. Rev. Lett.* **1996,** *77* 3865-3868

23. Blöchl, P. E., Projector Augmented-Wave Method. *Phys. Rev. B* **1994,** *50* 17953-17979.

24. Heyd, J.; Peralta, J. E.; Scuseria, G. E.; Martin, R. L., Energy Band Gaps and Lattice Parameters Evaluated with the Heyd-Scuseria-Ernzerhof Screened Hybrid Functional. *J. Chem. Phys.* **2005,** *123* 174101.

25. Dudarev, S. L.; Botton, G. A.; Savrasov, S. Y.; Humphreys, C. J.; Sutton, A. P., Electron-Energy-Loss Spectra and the Structural Stability of Nickel Oxide: An LSDA+*U* Study. *Phys. Rev. B* **1998,** *57* 1505-1509.

26. Scanlon, D. O.; Walsh, A.; Morgan, B. J.; Watson, G. W., An Ab Initio Study of Reduction of V_2O_5 through the Formation of Oxygen Vacancies and Li Intercalation. *J Phys. Chem. C* **2008,** *112* 9903-9911.

27. Nolan, M.; Watson, G. W., Hole Localization in Al Doped Silica: A DFT+U Description. *J. Chem. Phys.* **2006,** *125* 144701.

28. Scanlon, D. O.; Walsh, A.; Morgan, B. J.; Nolan, M.; Fearon, J.; Watson, G. W., Surface Sensitivity in Lithium-Doping of MgO: A Density Functional Theory Study with Correction for on-Site Coulomb Interactions. *J Phys. Chem. C* **2007,** *111* 7971-7979.

29. Scanlon, D. O.; Watson, G. W.; Payne, D. J.; Atkinson, G. R.; Egdell, R. G.; Law, D. S. L., Theoretical and Experimental Study of the Electronic Structures of MoO_3 and MoO_2. *J Phys. Chem. C* **2010,** *114* 4636-4645.

30. Morgan, B. J.; Scanlon, D. O.; Watson, G. W., Small Polarons in Nb- and Ta-Doped Rutile and Anatase TiO_2. *J. Mater. Chem.* **2009,** *19* 5175-5178.

31. Morgan, B. J.; Watson, G. W., A DFT+*U* Study of Oxygen Vacancy Formation at the (110), (100), (101) and (001) Surfaces of Rutile TiO_2. *J Phys. Chem. C* **2009,** *113* 7322-7328.

32. Keating, P. R. L.; Scanlon, D. O.; Morgan, B. J.; Galea, N. M.; Watson, G. W., Analysis of Intrinsic Defects in CeO_2 Using a Koopmans-Like GGA + U Approach. *J Phys. Chem. C* **2012,** *116* 2443-2452.

33. Scanlon, D. O.; Galea, N. M.; Morgan, B. J.; Watson, G. W., Reactivity on the (110) Surface of Ceria: A GGA + U Study of Surface Reduction and the Adsorption of CO and NO_2. *J Phys. Chem. C* **2009,** *113* 11095-11103.

34. Arnold, T.; Payne, D. J.; Bourlange, A.; Hu, J. P.; Egdell, R. G.; Piper, L. F. J.; Colakerol, L.; Masi, A.; Glans, P. A.; Learmonth, T.; Smith, K. E.; Guo, J.; Scanlon, D. O.;

Walsh, A.; Morgan, B. J.; Watson, G. W., X-Ray Spectroscopic Study of the Electronic Structure of $CuCrO_2$. *Phys. Rev. B* **2009,** *79* 075102.

35. Scanlon, D. O.; Walsh, A.; Morgan, B. J.; Watson, G. W.; Payne, D. J.; Egdell, R. G., Effect of Cr Substitution on the Electronic Structure of $CuAl_{1-x}Cr_xO_2$. *Phys. Rev. B* **2009,** *79* 035101

36. Fabris, S.; Vicario, G.; Balducci, G.; de Gironcoli, S.; Baroni, S., Electronic and Atomistic Structures of Clean and Reduced Ceria Surfaces. *J Phys. Chem. B* **2005,** *109* 22860-22867.

37. Fabris, S.; de Gironcoli, S.; Baroni, S.; Vicario, G.; Balducci, G., Taming Multiple Valency with Density Functionals: A Case Study of Defective Ceria. *Phys. Rev. B* **2005,** *71* 041102.

38. Murnaghan, F. D., The Compressibility of Media under Extreme Pressures. *Proc. Natl. Acad. Sci. USA* **1944,** *30* 244-247.

39. Allen, J. P.; Scanlon, D. O.; Parker, S. C.; Watson, G. W., Tin Monoxide: Structural Prediction from First Principles Calculations with Van Der Waals Corrections. *J. Phys. Chem. C* **2011,** *115* 19916-19924.

40. Panda, S. K.; Bhowal, S.; Delin, A.; Eriksson, O.; Dasgupta, I., Effect of Spin Orbit Coupling and Hubbard U on the Electronic Structure of IrO_2. *Phys. Rev. B* **2014,** *89* 155102.

41. Joyce, J. J.; Wills, J. M.; Durakiewicz, T.; Butterfield, M. T.; Guziewicz, E.; Sarrao, J. L.; Morales, L. A.; Arko, A. J.; Eriksson, O., Photoemission and the Electronic Structure of $PuCoGa_5$. *Phys. Rev. Lett.* **2003,** *91* 176401.

42. Arranz, A.; Sanchez-Royo, J. F.; Avila, J.; Perez-Dieste, V.; Asensio, M. C., Experimental Photohole Lifetimes Derived from Two-Dimensional States in Ag(111) Films

Deposited onto H-Passivated Si(111)-(1 X 1) Surfaces. *Surface Review and Letters* **2002,** *9* 729-734.

43. Norris, C. P., *Surface Science: New Research* **2005** Nova Scientific Publishers: Hauppauge New York.

44. Zhao, Z.; Li, Z.; Zou, Z., Electronic Structure and Optical Properties of Monoclinic Clinobisvanite $BiVO_4$. *Phys. Chem. Chem. Phys.* **2011,** *13* 4746-4753.

45. Spaldin, N. A., *Magnetic Materials : Fundamentals and Applications* (2nd ed.) **2010** Cambridge University Press, Cambridge.

46. Walsh, A.; Watson, G. W., The Origin of the Stereochemically Active Pb(II) Lone Pair: DFT Calculations on PbO and PbS. *J. Solid State Chem.* **2005,** *178* 1422-1428.

47. Walsh, A.; Watson, G. W., Influence of the Anion on Lone Pair Formation in Sn(II) Monochalcogenides: A DFT Study. *J. Phys. Chem. B* **2005,** *109* 18868-18875.

48. Watson, G. W.; Parker, S. C., Origin of the Lone Pair of a-Pbo from Density Functional Theory Calculations. *J. Phys. Chem. B* **1999,** *103* 1258-1262.

49. Watson, G. W.; Parker, S. C.; Kresse, G., *Ab Initio* Calculation of the Origin of the Distortion of α-PbO. *Phys. Rev. B* **1999,** *59* 8481-8486.

50. Payne, D. J.; Robinson, M. D. M.; Egdell, R. G.; Walsh, A.; McNutty, J.; Smith, K. E., The Nature of Electron Lone Pairs in $BiVO_4$. *Appl. Phys. Lett.* **2011,** *98* 212110.

51. Kudo, A.; Omori, K.; Kato, H., A Novel Aqueous Process for Preparation of Crystal Form-Controlled and Highly Crystalline $BiVO_4$ Powder from Layered Vanadates at Room Temperature and its Photocatalytic and Photophysical Properties. *J. Am. Chem. Soc.* **1999,** *121* 11459-11467.

52. Luo, H.; Mueller, A. H.; McCleskey, T. M.; Burrell, A. K.; Bauer, E.; Jia, Q. X., Structural and Photochemical Properties of $BiVO_4$ Thin Films. *J. Phys. Chem. C* **2008,** *112* 6099-6102.

53. Shannon, R. D., Revised Effective Ionic-Radii and Systematic Studies of Interatomic Distances in Halides and Chalcogenides. *Acta Cryst. A* **1976,** *32* 751-767.

54. Yeh, J. J.; Lindau, I., Atomic Subshell Photoionization Cross-Sections and Asymmetry Parameters $1 \leq Z \leq 103$. *At. Data Nucl. Data Tables* **1985,** *32* 1-155.

55. Payne, D. J.; Egdell, R. G.; Law, D. S. L.; Glans, P. A.; Learmonth, T.; Smith, K. E.; Guo, J. H.; Walsh, A.; Watson, G. W., Experimental and Theoretical Study of the Electronic Structures of α-PbO and β-PbO_2. *J. Mater. Chem.* **2007,** *17* 267-277.

56. Payne, D. J.; Paolicelli, G.; Offi, F.; Panaccione, G.; Lacovig, P.; Beamson, G.; Fondacaro, A.; Monaco, G.; Vanko, G.; Egdell, R. G., A Study of Core and Valence Levels in β-PbO_2 by Hard X-Ray Photoemission. *J. Electron Spectrosc. Relat. Phenom.* **2009,** *169* 26-34.

57. Payne, D. J.; Egdell, R. G.; Paolicelli, G.; Offi, F.; Panaccione, G.; Lacovig, P.; Monaco, G.; Vanko, G.; Walsh, A.; Watson, G. W.; Guo, J.; Beamson, G.; Glans, P. A.; Learmonth, T.; Smith, K. E., Nature of Electronic States at the Fermi Level of Metallic β-PbO_2 Revealed by Hard X-Ray Photoemission Spectroscopy. *Phys. Rev. B* **2007,** *75* 153102.

58. Korber, C.; Krishnakumar, V.; Klein, A.; Panaccione, G.; Torelli, P.; Walsh, A.; Da Silva, J. L. F.; Wei, S. H.; Egdell, R. G.; Payne, D. J., Electronic Structure of In_2O_3 and Sn-Doped In_2O_3 by Hard X-Ray Photoemission Spectroscopy. *Phys. Rev. B* **2010,** *81* 165207.

59. Mudd, J. J.; Lee, T.-L.; Muñoz-Sanjosé, V.; Zúñiga-Pérez, J.; Payne, D. J.; Egdell, R. G.; McConville, C. F., Valence-Band Orbital Character of CdO: A Synchrotron-Radiation

Photoemission Spectroscopy and Density Functional Theory Study. *Phys. Rev. B* **2014,** *89* 165305.

60. Drube, W.; Grehk, T. M.; Thieß, S.;Pradhan, G. B.; Varma, H. R.; P. C. Deshmukh, P.C.; Manson, S.T., Pronounced Effects of Interchannel Coupling in High Energy Photoionization. *J. Phys. B: At. Mol. Opt. Phys.* **2013** *46*, 245006

61. Thornton, G.; Dempsey, M. J., Final-State Effects in the 3d and 4d X-Ray Photoelectron-Spectra of CeO_2. *Chem. Phys. Lett.* **1981,** *77* 409-412.

62. Fujimori, A., Mixed-Valent Ground-State of CeO_2. *Phys. Rev. B* **1983,** *28* 2281-2283.

63. Kotani, A.; Mizuta, H.; Jo, T.; Parlebas, J. C., Theory of Core Photoemission Spectra in CeO_2. *Solid State Communications* **1985,** *53* 805-810.

64. Kotani, A., Theoretical Studies on Core-Level Spectra of Solids. *Journal Of Electron Spectroscopy And Related Phenomena* **1996,** *78* 7-12.

65. Kotani, A.; Ogasawara, H., Theory of Core-Level Spectroscopy of Rare-Earth-Oxides. *Journal of Electron Spectroscopy and Related Phenomena* **1992,** *60* 257-299.

66. Kotani, A.; Ogasawara, H., Interplay between Intra-Atomic Multiplet Coupling and Interatomic Hybridization in Core-Level Spectroscopy. *Journal of Electron Spectroscopy and Related Phenomena* **1997,** *86* 65-72.

67. Shannon, R. D.; Prewitt, C. T., Effective Ionic Radii in Oxides and Fluorides. *Acta Crystallographica Section B-Structural Crystallography and Crystal Chemistry* **1969,** *B 25* 925-946.

Table 1. Experimental unit cell and magnetic parameters for $CeVO_4$ and $Ce_{0.5}Bi_{0.5}VO_4$.

	$CeVO_4$		$Ce_{0.5}Bi_{0.5}VO_4$
Unit Cell Parameter	Present work	Published[18]	Present work
a (Å)	7.4001(2)	7.4002(1)	7.3550(2)
b(Å)	7.4001(2)	7.4002(1)	7.3550(2)
c (Å)	6.4992(2)	6.4972(1)	6.4796(2)
Volume ($Å^3$)	355.91(5)	355.78(2)	350.52(5)
Magnetic	Present work	Published[19]	Present work
μ_{eff} (μ_B)	2.89	2.64	3.23
θ (K)	-264	-109	-136

Table 2. Calculated structural data for MVO_4 (where M = Bi or Ce) with experimental values for comparison. Values in parentheses indicate percentage difference to experiment. The internal parameters for O, u_O and v_O, are only applicable to $CeVO_4$, where O atoms occupy the site at (0, u_O, v_O).

	$BiVO_4$		$CeVO_4$	
	Calculated	Experimental[12]	Calculated	Experimental[18]
$E_{AFM} - E_{FM}$ (eV)	-	-	-0.0005	-
a (Å)	5.192 (-0.10)	5.197	7.524 (+1.68)	7.400
b(Å)	5.190 (+1.84)	5.096	7.524 (+1.68)	7.400
c (Å)	11.783 (+0.69)	11.702	6.560 (+0.97)	6.497
Volume (Å^3)	317.51 (+2.45)	309.91	371.33 (+4.37)	355.78
u_O	-	-	0.07206	0.07210
v_O	-	-	0.20493	0.20670
M-O (Å)	2.506 (+6.82) 2.447 (+3.03) 2.449 (-3.13) 2.511 (-3.61)	2.346 2.375 2.528 2.605	2.480 (+1.56) 2.545 (+0.79)	2.442 2.525
V-O (Å)	1.758 (+0.80) 1.760 (+0.74)	1.744 1.747	1.743 (+1.87)	1.711
$M \cdots M$ (Å)	3.924 (+4.28)	3.763	4.104 (+1.56)	4.041

Table 3. Calculated structural data for monoclinic and tetragonal $Ce_{0.5}Bi_{0.5}VO_4$. . Bond lengths follow the same order as those in Table 1 for the respective cells.

	Monoclinic $Ce_{0.5}Bi_{0.5}VO_4$	Tetragonal $Ce_{0.5}Bi_{0.5}VO_4$
$E_{AFM} - E_{FM}$ (eV)	0.0694	-0.3655
a (Å)	5.218	7.477
b(Å)	5.213	7.477
c (Å)	11.866	6.508
Volume (Å^3)	322.74	363.80
Ce-O (Å)	2.532 2.489 2.489 2.532	2.453 2.547
Bi-O (Å)	2.503 2.469 2.461 2.524	2.440 2.520
V-O (Å)	1.752 1.755	1.74431

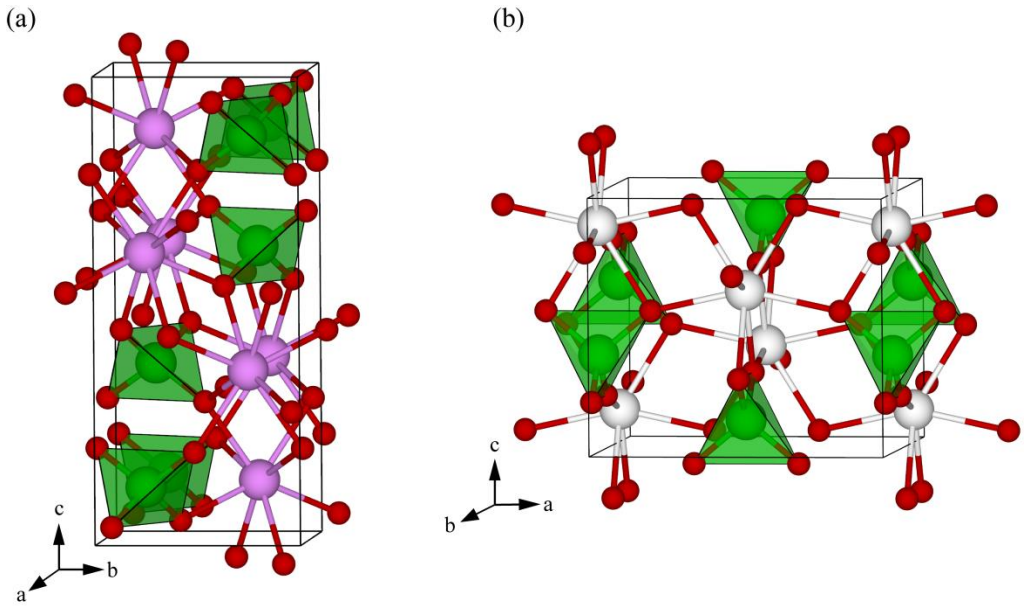

Figure 1. Unit cells structures of (a) $BiVO_4$ and (b) $CeVO_4$. Bi, Ce, V and O atoms are coloured purple, siver, green and red, respectively. Polyhedra are shown on VO_4 subunits for clarity.

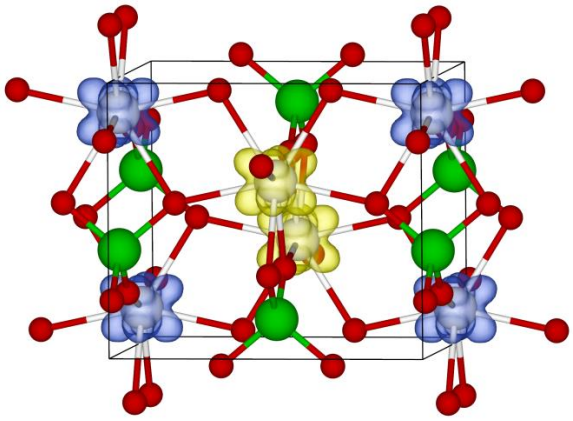

Figure 2. Spin density plot for the unit cell structure of $CeVO_4$, indicating the magnetic ground state. The antiferromagnetic ordering is indicated by the yellow and blue isosurfaces, spin up and spin down, respectively, at a level of 0.05 electrons $Å^{-3}$. The localisation of unpaired spin density exclusively on Ce ions confirms the compound should be described as $Ce(III)V(V)O_4$ rather than $Ce(IV)V(IV)O_4$.

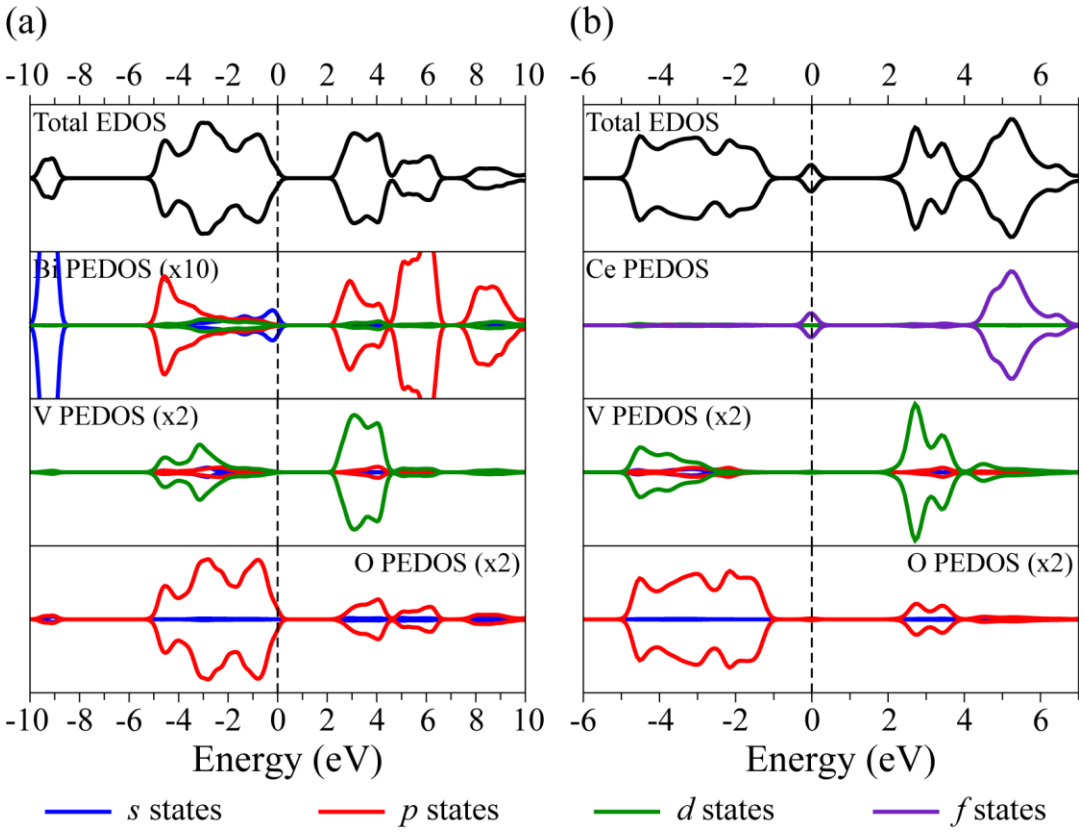

Figure 3. Calculated density of states for (a) $BiVO_4$ and (b) $CeVO_4$. The valence band maximum is set to 0.0eV and the *s*, *p*, *d* and *f* states are coloured blue, red, green and purple, respectively.

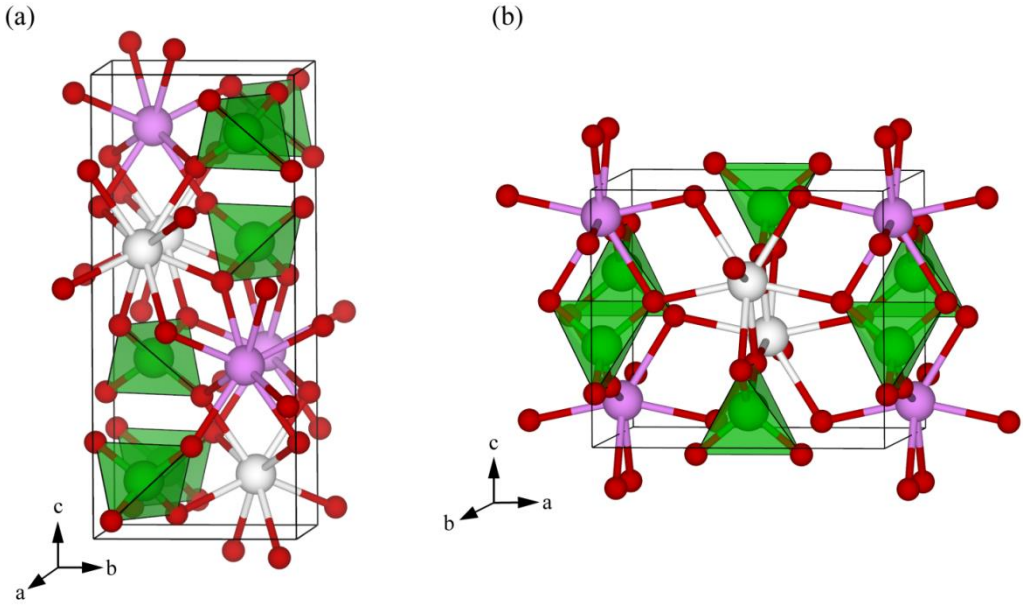

Figure 4. Unit cells structures of **(a)** monoclinic $Ce_{0.5}Bi_{0.5}VO_4$ and **(b)** tetragonal $Ce_{0.5}Bi_{0.5}VO_4$. Bi, Ce, V and O atoms are coloured purple, white, green and red, respectively. Polyhedra are shown on VO_4 subunits for clarity.

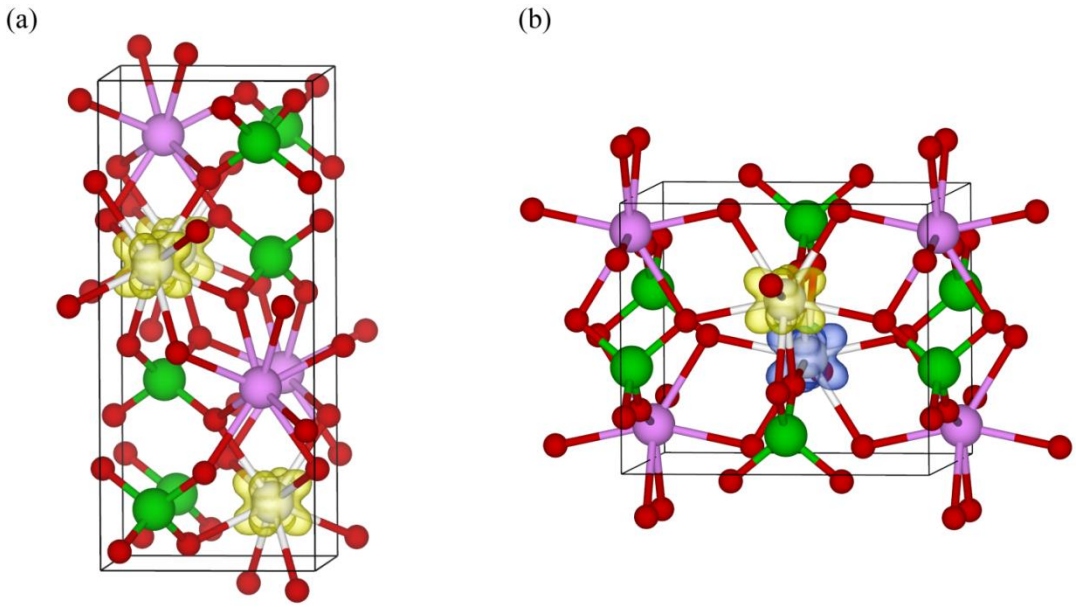

Figure 5. Calculated spin density plots for **(a)** monoclinic $Ce_{0.5}Bi_{0.5}VO_4$ and **(b)** tetragonal $Ce_{0.5}Bi_{0.5}VO_4$ indicating the magnetic ground state. Excess up and down spin are indicated by the yellow and blue isosurfaces, up and down spin, respectively, at a level of 0.05 electrons $Å^{-3}$.

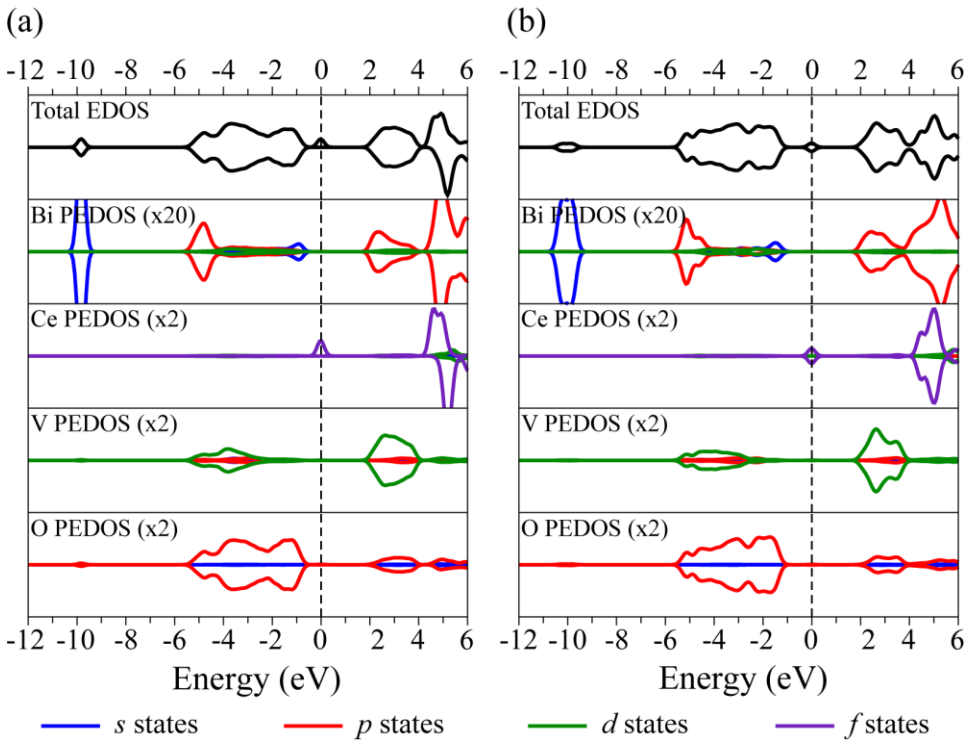

Figure 6. Calculated density of states (a) monoclinic $Ce_{0.5}Bi_{0.5}VO_4$ and (b) tetragonal $Ce_{0.5}Bi_{0.5}VO_4$. The valence band maximum is set to 0.0eV and the *s*, *p*, *d* and *f* states are coloured blue, red, green and purple, respectively.

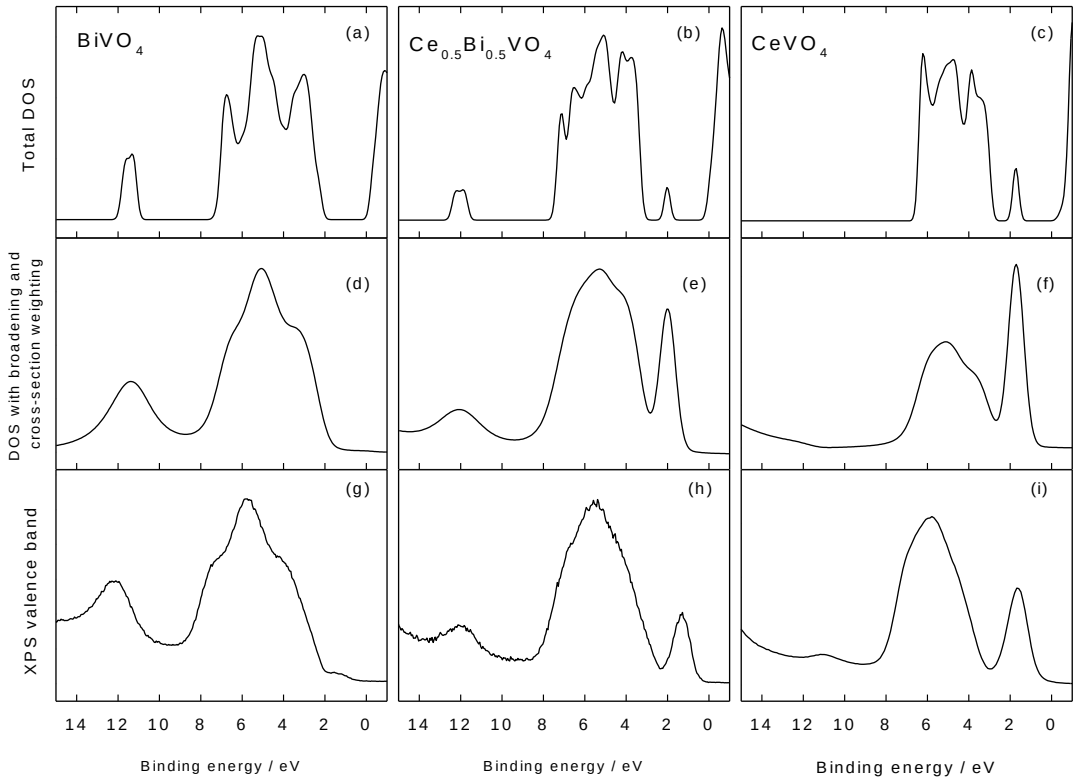

Figure 7 Panels (a), (b) and (c) show total electronic densities of states derived from bandstructure calculations for $BiVO_4$, $Ce_{0.5}Bi_{0.5}VO_4$ and $CeVO_4$. Panels (d), (e) and (f) show broadened densities of states with different orbital contributions weighted by ionisation cross sections tabulated by Yeh and Lindau[54]. Panels (g), (h) and (i) show corresponding valence band X-ray photoemission spectra. Binding energies are defined relative to the bottom of the conduction band.

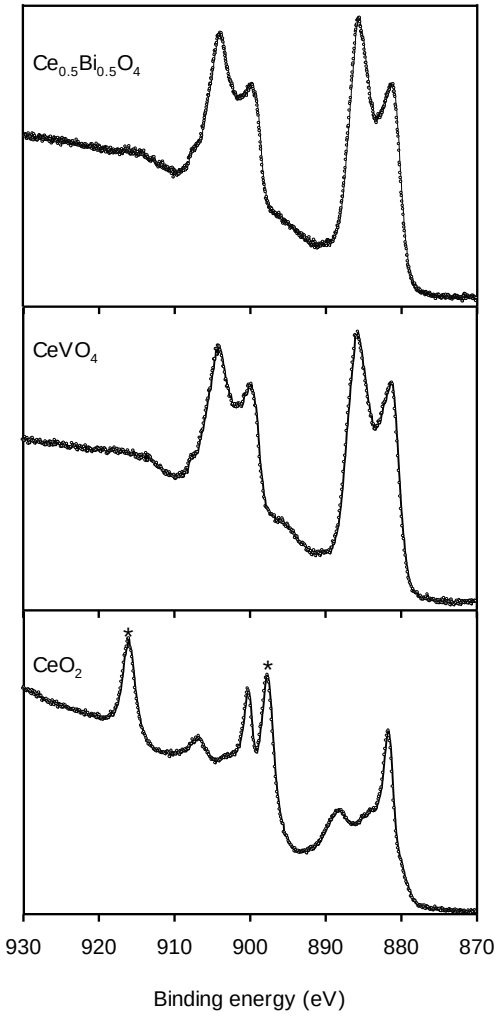

Figure 8. Ce 3d core level photoemission spectra of $Ce_{0.5}Bi_{0.5}VO_4$, $CeVO_4$ and CeO_2. The peaks highlighted with * in the spectra of CeO_2 correspond to the $3d_{5/2}$ and $3d_{3/2}$ components of the $4f^0$ final state.

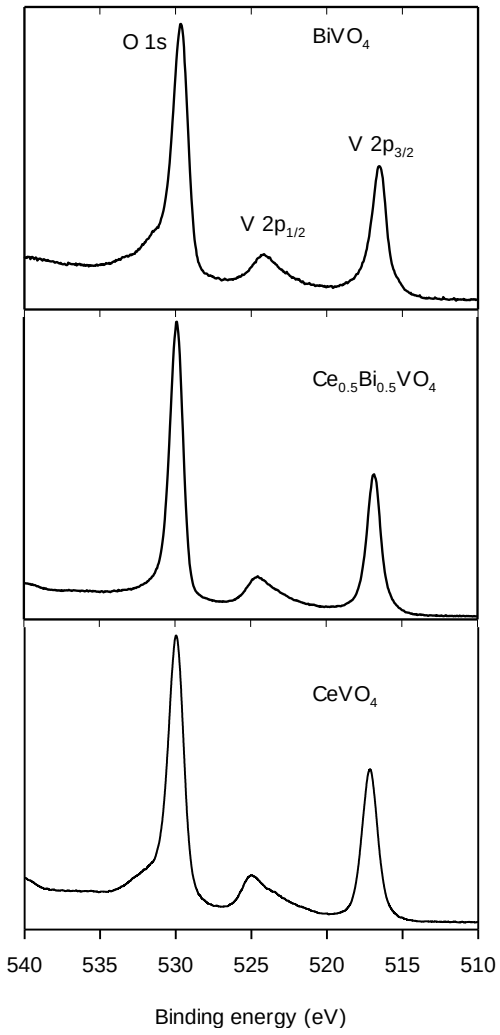

Figure 9. V 2*p* and O1*s* core level photoemission spectra of $BiVO_4$, $Ce_{0.5}Bi_{0.5}VO_4$ and $CeVO_4$.

Table of Contents Image